

# The Thermal Distortion of a Funnel Mold

LANCE C. HIBBELER, BRIAN G. THOMAS, RONALD C. SCHIMMEL,  
and GERT ABBEL

This article investigates the thermal distortion of a funnel mold for continuous casting of thin slabs and explores the implications on taper and solidification of the steel shell. The three-dimensional mold temperatures are calculated using shell-mold heat flux and cooling water profiles that were calibrated with plant measurements. The thermal stresses and distorted shape of the mold are calculated with a detailed finite-element model of a symmetric fourth of the entire mold and waterbox assembly, and they are validated with plant thermocouple data and measurements of the wear of the narrow-face copper mold plates. The narrow-face mold distorts into the typical parabolic arc, and the wide face distorts into a “W” shape owing to the large variation in bolt stiffnesses. The thermal expansion of the wide face works against the applied narrow-face taper and funnel effects, so the effect of thermal distortion must be considered to accurately predict the ideal mold taper.

DOI: 10.1007/s11663-012-9696-5

© The Minerals, Metals & Materials Society and ASM International 2012

## I. INTRODUCTION

THE thermal distortion of the continuous casting mold from room temperature to steady operating temperatures can influence the behavior of the solidifying steel strand in many ways, but likely the most important of these is the narrow-face taper. Mold distortion has been investigated in billet molds,<sup>[1–6]</sup> conventional thick-slab molds,<sup>[7–9]</sup> beam-blank molds,<sup>[10]</sup> and thin-slab molds with<sup>[11–13]</sup> and without<sup>[12,13]</sup> a funnel. Each mold shape has distinctive thermomechanical behavior, but in general, these studies have revealed the importance of the waterbox on the mechanical behavior of the system,<sup>[7]</sup> and the importance of mold distortion on mold taper,<sup>[2,5]</sup> mold cracks,<sup>[11,13]</sup> and steel strand cracks.<sup>[3,4]</sup>

Distortion is less severe with lower mold temperatures, such as those caused by lower casting speeds<sup>[2,4]</sup> or thinner mold plates.<sup>[2,8]</sup> Coating layers have little influence on the mechanical behavior of the mold<sup>[8]</sup> because they are so thin. The highest temperature is generally found just below the meniscus; operating a caster with a metal level near a row of bolts increases inelastic deformation of the copper near the hot face.<sup>[2]</sup> Many previous mold distortion models assume elastic behavior. Incorporating inelastic behavior of the mold copper is needed to predict residual stresses and residual distortion, but it does not significantly affect the mold shape during operation.<sup>[11]</sup> Previous models often oversimplify important effects such as bolts, clamping,

interfacial contact, and mesh resolution, but their largest deficiency is oversimplification of the mold and waterbox geometry. A complete quantitative analysis of thermal distortion during operation of a funnel mold, including realistic heat transfer, all of the important geometric details, proper constraints, shell/mold friction, and validation with plant measurements, has not yet been performed and is the aim of this study.

## II. MOLD GEOMETRY

The main geometric features of the funnel-shaped mold and waterbox under consideration are shown in Figures 1 through 3. Although the waterbox is not perfectly symmetrical, only one fourth of the assembly was modeled. Asymmetric effects, such as variations in bolt tightening or mold alignment, and mold geometry changes to accommodate the level detector on one side are expected to be small. This mold has no coating layers. Except for the top row, each bolt is instrumented with a thermocouple set 20 mm from the hot face.

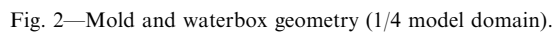
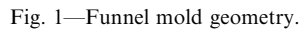
Each narrow-face copper plate is cooled by four 14-mm diameter cylindrical water tubes. The hot face of the narrow face is curved slightly concave towards the molten steel to ensure that any bulging of the strand during soft reduction below the mold is outward. Each narrow face is attached with a column of bolts with 134-mm spacing to a waterbox that is suspended by large hooks on two support cylinders, which may be dynamically positioned to adjust mold width and taper.

The funnel opening on the wide face decreases from 136.8 mm at mold top to 106 mm at mold exit. The wide-face water channels are 5 mm wide by 15 mm deep, cut with a ball end mill, and set 20 mm from the hot face with 10 mm spacing in banks of 18. The inlets and outlets of the water channels curve away from the hot face to meet the waterbox. Each wide face has a rectangular array of 81 bolts spaced 125 mm apart in the

---

LANCE C. HIBBELER, Graduate Student, and BRIAN G. THOMAS, Professor, are with the Department of Mechanical Science and Engineering, University of Illinois at Urbana-Champaign, Urbana, IL 61802. Contact e-mail: bgthomas@illinois.edu. RONALD C. SCHIMMEL, Senior Process Engineer, is with Strip Mainland Europe DSP, Tata Steel, 1970 CA, IJmuiden, The Netherlands. GERT ABBEL, Knowledge Group Leader, is with Research, Development, and Technology, Tata Steel.

Manuscript submitted November 22, 2011.



by 650-mm cavities to accommodate an electromagnetic flow control system.

Heat transport is governed by the conservation of energy, a partial differential equation that simplifies when modeling mold behavior during steady casting.

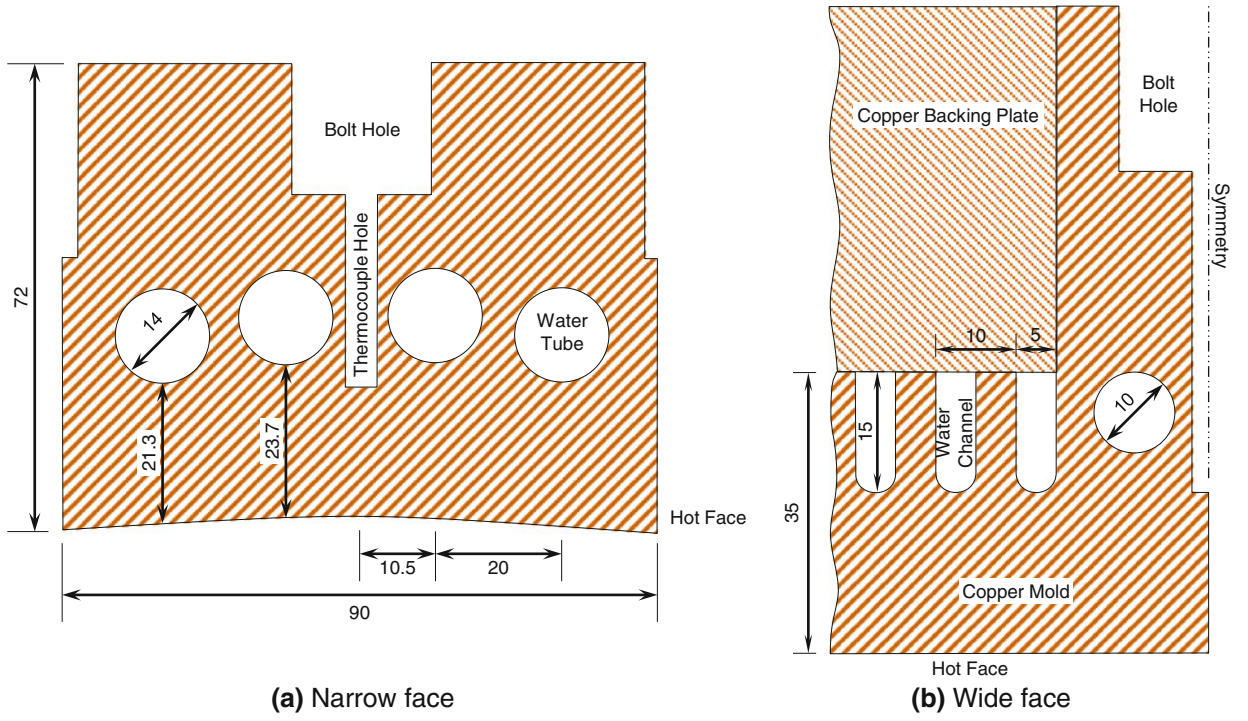


Fig. 3—Water channel details: (a) narrow face and (b) wide face.

The temperature distribution is found as a function of the three coordinate directions  $T(\mathbf{x})$  by solving

$$\nabla \cdot (k \cdot \nabla T) = 0 \quad [1]$$

where  $k$  is the isotropic thermal conductivity. The boundary conditions on each portion of the domain surface include either

$$-k (\nabla T) \cdot \mathbf{n} = q^{\text{sp}} \quad [2]$$

where  $q^{\text{sp}}(\mathbf{x})$  is the specified heat flux in the direction of the outward-pointing surface normal  $\mathbf{n}(\mathbf{x})$ , or:

$$-k (\nabla T) \cdot \mathbf{n} = h (T - T_{\infty}) \quad [3]$$

where  $h(\mathbf{x})$  is the convection heat-transfer coefficient and  $T_{\infty}(\mathbf{x})$  is the ambient temperature.

Ignoring gravity, the mechanical behavior is governed by momentum equilibrium

$$\nabla \cdot \boldsymbol{\sigma} = 0 \quad [4]$$

where  $\boldsymbol{\sigma}(\mathbf{x})$  is the Cauchy stress tensor, computed from Hooke's law for linear elasticity

$$\boldsymbol{\sigma} = \mathbf{C} : \boldsymbol{\varepsilon}^{\text{el}} \quad [5]$$

The components of the fourth-rank elastic stiffness tensor  $\mathbf{C}$  for isotropic materials are defined as

$$C_{ijkl} = \frac{E}{2(1+\nu)} (\delta_{ik}\delta_{jl} + \delta_{il}\delta_{jk}) + \frac{\nu E}{(1+\nu)(1-2\nu)} \delta_{ij}\delta_{kl} \quad [6]$$

where  $E$  is Young's modulus,  $\nu$  is Poisson's ratio, and  $\delta_{ij}$  is the Kronecker delta (1 if  $i = j$  and 0 otherwise).

The elastic strain tensor  $\boldsymbol{\varepsilon}^{\text{el}}(\mathbf{x})$  is computed from an additive decomposition of the strains

$$\boldsymbol{\varepsilon}^{\text{el}} = \boldsymbol{\varepsilon} - \boldsymbol{\varepsilon}^{\text{th}} \quad [7]$$

where  $\boldsymbol{\varepsilon}(\mathbf{x})$  is the total strain tensor, computed from the gradient of the displacement field  $\mathbf{u}(\mathbf{x})$  assuming small strain

$$\boldsymbol{\varepsilon} = \frac{1}{2} (\nabla \mathbf{u} + (\nabla \mathbf{u})^T) \quad [8]$$

and  $\boldsymbol{\varepsilon}^{\text{th}}(\mathbf{x})$  is the thermal strain tensor, calculated for isotropic materials using the coefficient of thermal expansion  $\alpha$  and the temperature above a reference temperature  $T_0$

$$\boldsymbol{\varepsilon}^{\text{th}} = \alpha (T - T_0) \mathbf{I} \quad [9]$$

where  $\mathbf{I}$  is the second-rank identity tensor. Relevant mechanical boundary conditions include specifying the displacement vector  $\mathbf{u}^{\text{sp}}(\mathbf{x})$

$$\mathbf{u} = \mathbf{u}^{\text{sp}} \quad [10]$$

or the traction vector  $\mathbf{T}^{\text{sp}}(\mathbf{x})$ :

$$\boldsymbol{\sigma} \cdot \mathbf{n} = \mathbf{T}^{\text{sp}} \quad [11]$$

The finite-element method was employed to solve the equations, using the commercial software ABAQUS.<sup>[14]</sup> Owing to the weak coupling between the thermal and mechanical behavior of the mold, the analysis was performed as two independent steps. A refined mesh of the complete three-dimensional (3-D) mold geometry, including the plates, water channels, bolts, bolt holes, tie



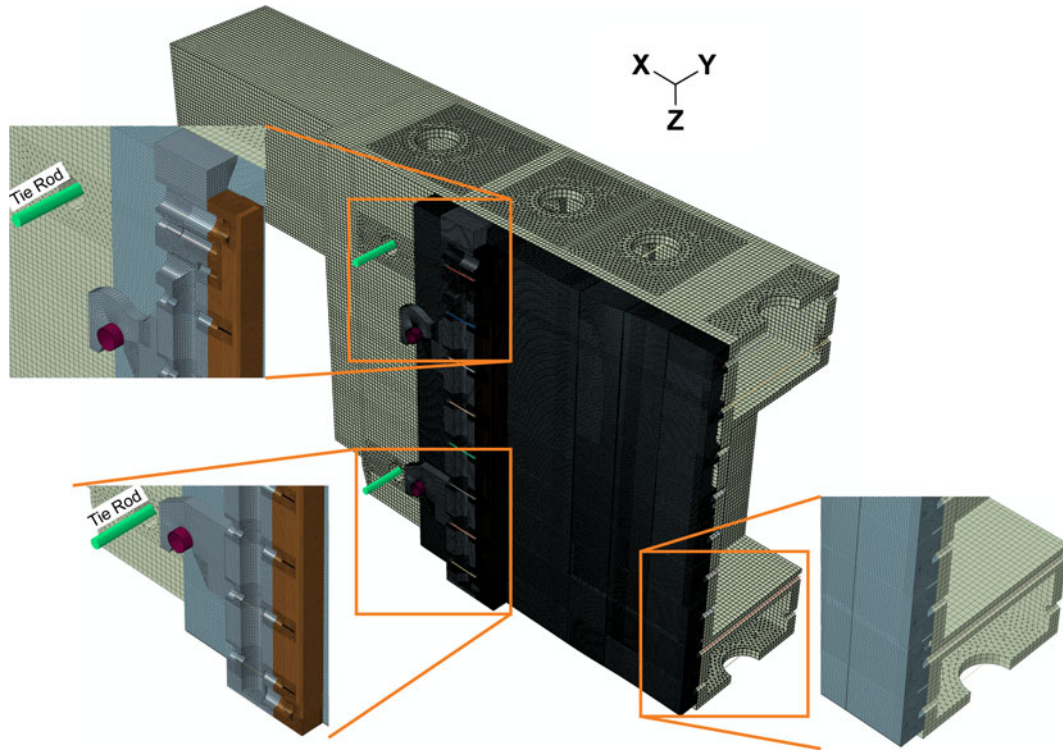


Fig. 4—Mold and waterbox assembly mesh.

**Table I. Computational Model Mesh Details**

Part	Nodes	Elements
Wide-face mold plate	855,235	4,223,072
Wide-face waterbox	185,534	190,457
Wide-face bolts	90	45
Tie rods	4	2
Narrow-face mold plate	233,931	495,566
Narrow-face waterbox	83,269	239,604
Narrow-face bolts	16	8
Total	1,358,079	5,148,754

rods, and waterboxes, was constructed of a mix of standard “fully integrated” linear 4-node tetrahedral, 6-node wedge, and 8-node hexahedral elements (ABAQUS diffusion-controlled 3-D elements DC3D4, DC3D6, and DC3D8 for the thermal problem and continuum 3-D elements C3D4, C3D6, and C3D8 for the mechanical problem). Numerical experiments with these elements in similar problems has shown them quite capable of matching analytical thermoelastic solutions, so numerical noise is of little concern. Details are provided in Figure 4 and Table I.

#### A. Heat-Transfer Model Details

For the thermal problem, a specified heat flux boundary condition was applied to the “active” areas of the hot-face surfaces in contact with the solidifying steel strand, which extend below the meniscus from the centerlines to the edges where the narrow- and wide-face

plates meet. A convection heat flux boundary condition was applied on the water channel surfaces with the convection heat-transfer coefficient calculated from Sleicher and Rouse<sup>[15]</sup>

$$\text{Nu} = 5 + 0.015\text{Re}^{0.88-0.24/(4+\text{Pr})}\text{Pr}^{1/3+0.5\exp(-0.6\text{Pr})} \quad [12]$$

where the Nusselt number  $\text{Nu} = hD_c/k_w$ , Prandtl number  $\text{Pr} = c_{pw}\mu_w/k_w$ , and Reynolds number  $\text{Re} = \rho_w V_w D_c / \mu_w$  are evaluated at the temperatures of the bulk water, the mold wall surface, and their average (“film temperature”), respectively. This correlation was chosen for its better fit with measurements, (7 pct average error) relative to other correlations such as Dittus-Boelter. The cooling water thermal conductivity  $k_w$ , mass density  $\rho_w$ , specific heat capacity  $c_{pw}$ , and dynamic viscosity  $\mu_w$  are all calculated as functions of temperature. The hydraulic diameter of the water channel  $D_c$ , defined as four times the cross-sectional area divided by the perimeter, is calculated from the appropriate geometry defined in Section II, and the water velocity  $V_w$  is chosen to match the plant.

The shell-mold heat flux profile, water channel convection heat-transfer coefficients, and water temperature varied with position down the mold, as shown in Figure 5 for the different mold pieces, according to the predictions of the continuous casting process model CONID<sup>[16]</sup> that was calibrated with plant data in previous work.<sup>[17]</sup> Specifically, the heat flux profile in Figure 5 represents an average heat removal of 2.7 MW/m<sup>2</sup>, which is close to the 2.8 MW/m<sup>2</sup>, measured during typical casting of a 0.045 wt pct C low-carbon, 90 × 1200 mm Al-killed and

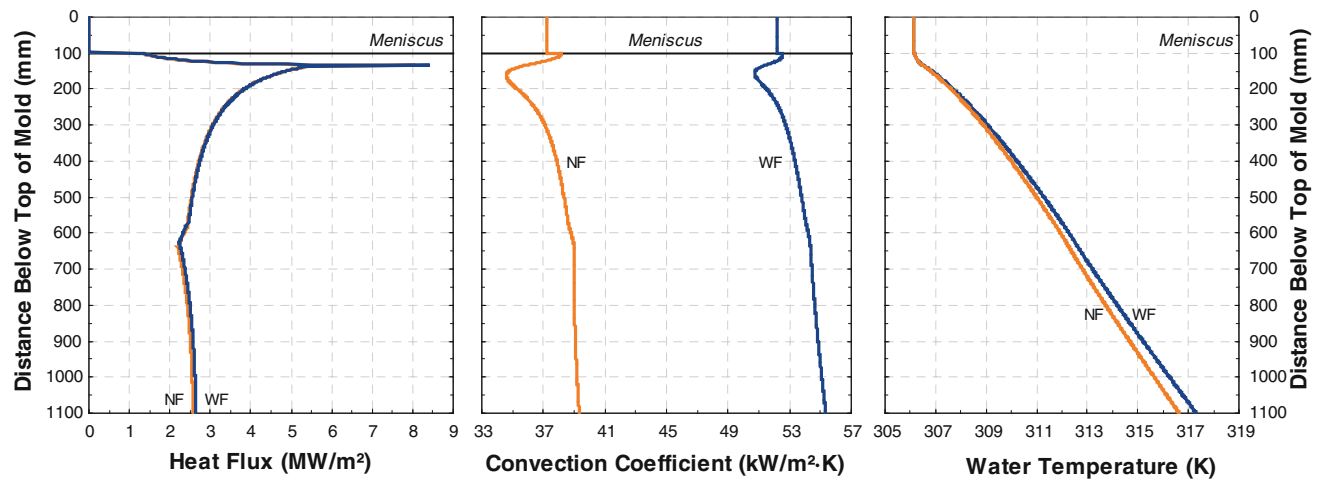


Fig. 5—Thermal boundary conditions as functions of distance down the mold.

Table II. Model Properties and Constants

Property or Constant	Value
Mold material	Cu-Cr-Zr alloy
Mold thermal conductivity	350 W/(m·K)
Mold Young's modulus	117 GPa
Mold Poisson's ratio	0.181
Mold coefficient of expansion	18 $\mu\text{m}/(\text{m}\cdot\text{K})$
Mold initial temperature	303 K (30 °C)
Waterbox material	AISI 316Ti SS
Waterbox Young's modulus	200 GPa
Waterbox Poisson's ratio	0.299
Mold-mold friction coefficient	1.0
Mold-waterbox friction coefficient	0.5
Liquid steel mass density	7100 kg/m <sup>3</sup>
Acceleration due to gravity	9.807 m/s <sup>2</sup>
Bolt friction coefficient	0.3
Bolt thread pitch	1.5 mm
Bolt tightening torque	100

Ca-treated steel slab cast at 5.5 m/min with 14 K (14 °C) superheat and 8.5 m/s water velocity. These heat flux data and convection coefficient and water temperature data were input to ABAQUS via user subroutines DFLUX and FILM, respectively. The constant material properties are given in Table II. All heat was assumed to be removed by the cooling water, so the waterboxes were not included in the thermal analysis. The interfaces between the mold pieces were modeled as thermally insulated because the thermal distortion causes gaps to open along most of the contacting surfaces. With 1,089,166 total degrees of freedom, this linear thermal problem required about 12 minutes to solve on an 8-core 2.66 GHz Intel Xeon processor (Intel, Santa Clara, CA) with 8 GB of RAM.

## B. Mechanical Model Details

In solving the force-equilibrium equations, the main driving force of the mechanical behavior of the mold is the thermal expansion, which was computed with Eq. [9]

according to the temperature distribution calculated in the thermal model, assuming a stress-free condition at the uniform initial temperature of 303 K (30 °C). The ferrostatic pressure, assumed to transmit through the solidifying steel shell and slag layer to the mold hot faces, was modeled as a pressure load  $T^{\text{sp}} = -p\mathbf{n}$  that increases with distance below the meniscus:

$$p = \begin{cases} 0 & z < 0 \\ \rho g z & z \geq 0 \end{cases} \quad [13]$$

where  $p$  is pressure,  $\rho$  is the mass density of the liquid steel,  $g$  is acceleration due to gravity, and  $z$  is distance below the meniscus in the casting direction. The pressure was applied on “active” areas of the hot face via an ABAQUS user subroutine DLOAD. The narrow-face support cylinders were modeled as “analytical rigid surfaces,” with mechanical contact defined between them and the appropriate surfaces on the waterbox hooks. The cylinders were constrained with zero-displacement boundary conditions to prevent rigid body motion of the narrow face. The large tie rods that hold the assembly together, the symmetry conditions  $\mathbf{u} \cdot \mathbf{n} = 0$  on appropriate planes, and the friction between the narrow and wide faces prevent rigid body motion of the wide face. The mechanical contact between portions of the contacting surfaces of the mold plates, and between each mold plate and its respective waterbox, was modeled using the standard “hard” contact algorithm within ABAQUS with the static friction coefficients given in Table II.

Each mold bolt was modeled as a truss element (axial extension degree-of-freedom only, ABAQUS element T3D2), and distributing coupling constraints (DCCs) were used to connect the endpoints of the truss elements to the appropriate surfaces on the molds and waterboxes, *i.e.*, the female bolt threads and the mold outer surface contacting the bolt head, as illustrated in Figure 6. The DCC distributes the behavior of the truss element endpoint over the designated surface in an average sense such that the force and moment balances are maintained. Each simulated bolt was given a stiffness based on its length and the effective stiffness

of the actual bolt, and it was prestressed according to plant practice. The wide face uses shorter bolts that only go through the backing plate and longer bolts that go through both the backing plate and stiffener plates or the mold water. Details of the simulated bolts are presented in Table III, including the prestress, and the great differences in bolt stiffness that arise mainly due to their different lengths. The bolt calculations performed here follow those done in previous work.<sup>[7]</sup> A mass density of 8900 kg/m<sup>3</sup> for the mold copper gives weights of 7.23 kN and 0.527 kN for the wide and narrow faces. Uniformly distributing these over the appropriate number of bolts, the average shearing stress due to the mold weight is 0.569 MPa and 0.364 MPa. These are negligible relative to the prestress, so the effect of gravity was neglected safely in the numerical model.

The full mold assembly includes four “tie rods,” indicated in Figure 4, that hold the assembly together and oppose the ferrostatic pressure and thermal distortion. Due to symmetry, only two of these were modeled. They were treated as prestressed truss elements with DCCs. The effective stiffness of the simulated tie rods includes the stiffness of the tie rods (133 MN/m) and of the packs of Belleville-washer disk springs (47.1 MN/m upper and 44.6 MN/m lower) to which clamping forces were applied as preloads. The details of the tie rods are also presented in Table III.

With 4,830,081 degrees of freedom, this nonlinear mechanical model took 44.6 days to solve on the same computer as the thermal problem. The large computational effort was due to both the large problem size and the iteration needed for convergence of the contact algorithm. To assist convergence, the model was

marched through pseudo-time, applying the thermal load in increasing increments over ten steps.

IV. MOLD HEAT-TRANSFER RESULTS

The calculated surface temperatures of the wide-face and narrow-face mold pieces are shown in Figures 7 and 8. The field is clearly three dimensional and is affected by both the cooling channels and the funnel geometry. Hot-face temperature profiles around the wide-face mold perimeter are shown in Figure 9 at various distances down the length of the mold. The hot face of the wide face shows temperature variations around its perimeter mainly because the vertical water tubes near the bolts are further from the hot face, and thus, they extract heat less efficiently than the channels. This causes regions beneath the bolt holes to be locally hotter by about 15 K (15 °C) over most of the length of the mold. The wider channel cut for the mold-level sensor also disturbs the uniformity of the surface temperatures, but this effect is much smaller than the change in cooling around the bolt columns.

The funnel geometry adds a very small two-dimensional effect to the heat extraction. The “inside-curve” region of the funnel surface (defined in Figure 1) extracts slightly *more* heat than the flat regions, resulting

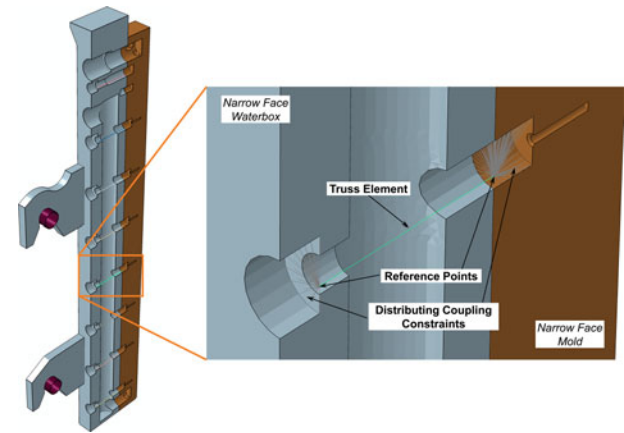


Fig. 6—Simulated mold bolt with distributing coupling constraint.

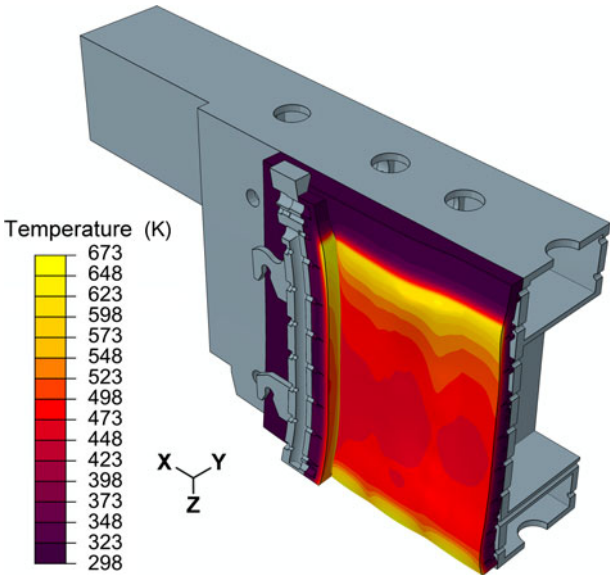


Fig. 7—Calculated mold temperature field (50 times scaled distortion).

Table III. Bolt and Tie Rod Details

Bolt	Length (mm)	Cross-Sectional Area (mm <sup>2</sup> )	Applied Torque (N·m)	Preload (kN)	Prestress (MPa)	Stiffness (MN/m)
NF (short)	150	181	100	30	168	240
WF short	87	187	100	30	162	424
WF long	449	143	100	30	212	63
Upper tie rod	1335	1215	—	40	33	34.8
Lower tie rod	1335	1215	—	70	58	33.4

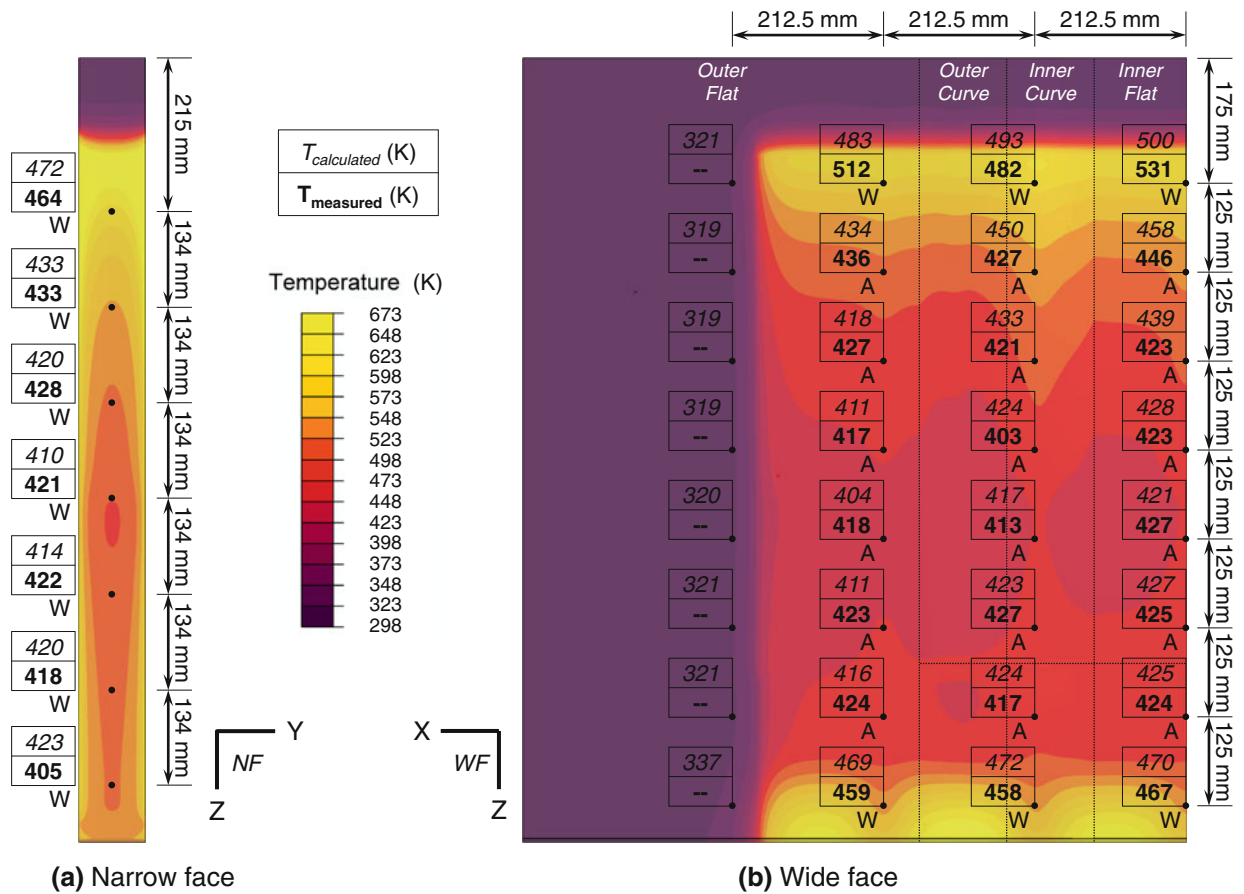


Fig. 8—Hot-face temperatures (contours) and thermocouple temperatures (boxes): (a) narrow face and (b) wide face.

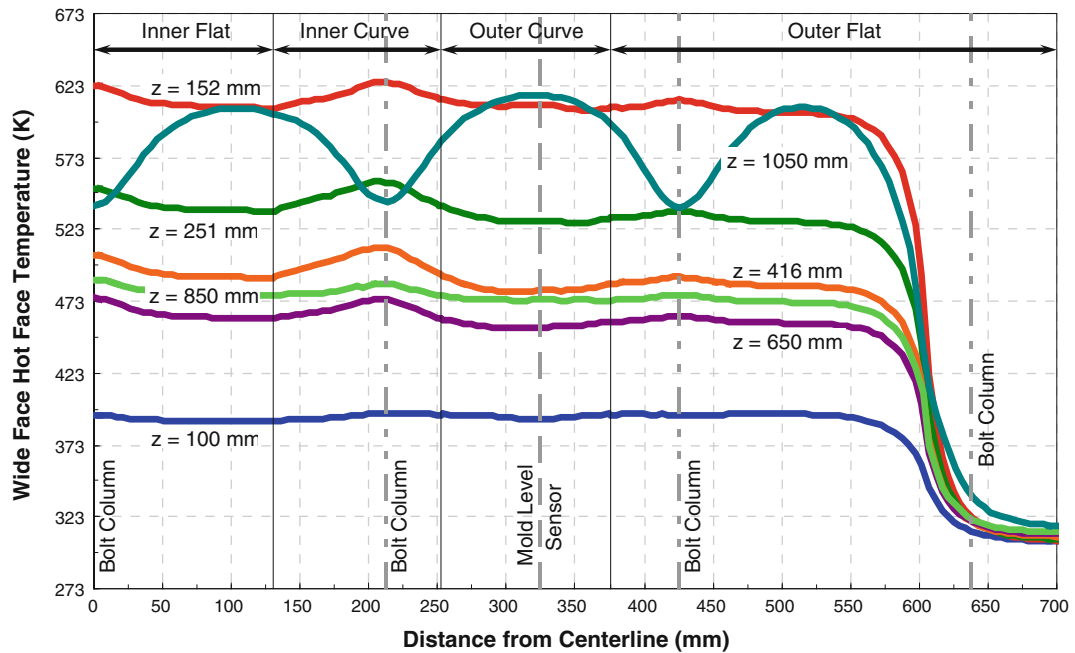


Fig. 9—Wide-face hot-face temperature profiles around the perimeter.

in a cooler shell and warmer mold by about 2 K (2 °C) (“diverging” heat flow). The outside-curve region of the funnel surface extracts slightly *less* heat, resulting in a

warmer shell and a cooler mold (“converging” heat flow). The funnel shape appears to have no other effect on heat transfer, owing to the constant distance of the



cooling channel roots from the hot face, even though the channels are cut perpendicular to the back face and not to the funnel itself.

The bottom portion of the mold shows much larger surface temperature variation (by more than 120 K (120 °C)) because the cooling channels cannot extend to the bottom of the mold, as pictured in Figure 10. This causes increasing temperature towards the mold bottom at the water channels, with peak temperatures of almost 623 K (350 °C), which is similar to the region of peak heat flux near the meniscus. This effect is less near the water tubes because they extend further down the mold than the curving water channels.

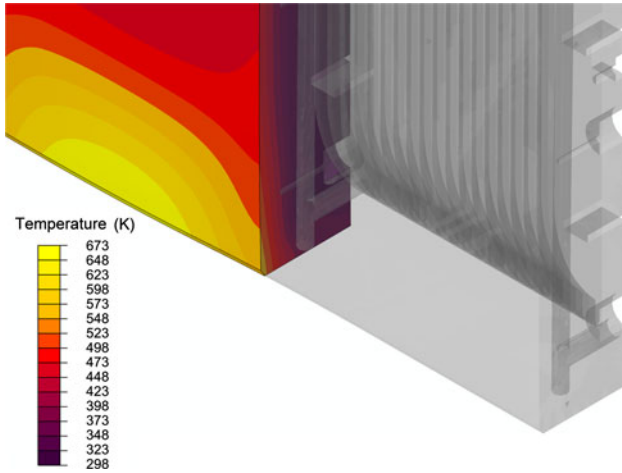


Fig. 10—Wide-face cooling channels near mold exit.

The surface temperature of the mold is locally higher by 10 K (10 °C) to 25 K (25 °C) near the center of the “inside-curve” region of the funnel for most of the length of the mold. This higher mold temperature and the resulting change in heat transfer across the shell-mold gap, especially near the meniscus, can lead to longitudinal facial cracks (LFCs) in the shell. This is because the temperature and heat-flux variations around the perimeter cause corresponding variations in the temperature and thickness of the solidifying steel shell, causing strain concentration and hot tears at the liquid films between the largest, weakest grain boundaries. Previous work<sup>[18,19]</sup> found more depression-style LFCs in this region due to shell bending caused by the funnel. The higher mold surface temperature of this region may exacerbate the problem. This important cracking mechanism deserves further study.

The temperature profile down the length of the narrow-face mold at the centerline is shown in Figure 11. The narrow face exhibits less variation of surface temperature around the perimeter because the cooling channel design is more uniform. Due to the concave shape of the narrow-face hot face, the extra copper between the water and the hot face serves to increase the mold hot-face temperature slightly towards the slab corners. This could contribute to “finning” defects and sticker breakouts due to inelastic squeezing of the narrow-face edges, according to the mechanism described in previous work.<sup>[7]</sup>

#### A. Thermocouple Temperature Validation

To further validate the model, the model predictions (top boxes) of thermocouple temperatures are compared against their measured values (bottom boxes) in

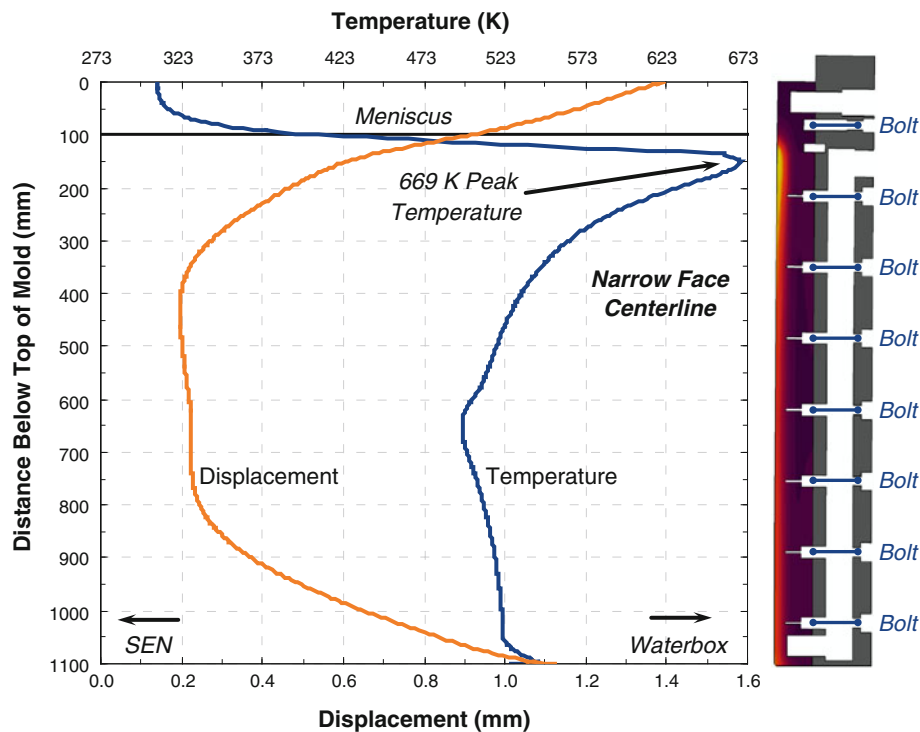


Fig. 11—Narrow-face hot-face centerline temperature and distortion.



Figure 8. Plant data were selected for conditions close to those modeled, except that the strand width was 1300 mm, contrasting with 1200 mm in the model. The model thus significantly underpredicts temperatures of the thermocouple column furthest from the centerline of the wide face, so these temperatures are not given.

The measured thermocouple temperatures were time averaged over 30 minutes of steady casting and then adjusted to account for heat removal through the thermocouple wires. Assuming the thermocouple and wire act as circular-cylindrical rod fins,<sup>[10]</sup> the adjusted temperature  $T'_{TC}$  is given by

$$T'_{TC} = T_{TC} + (T_{TC} - T_{amb}) \frac{d_{gap}}{k_{gap}} \frac{\sqrt{hDk_{TC}}}{D/2} \quad [14]$$

where  $T_{TC}$  is the measured thermocouple temperature,  $T_{amb}$  is the ambient temperature,  $d_{gap} = 0.01$  mm, and  $k_{gap} = 1.25$  W/m·K are the size and thermal conductivity of the gap assumed between the thermocouple tip and the mold copper,  $h$  is the heat-transfer coefficient along the rod,  $k_{TC} = 212$  W/m·K is the copper-constantan thermocouple thermal conductivity, and  $D = 4$  mm is the thermocouple wire diameter. The ambient temperature is taken from the CONID predictions of water temperature in Figure 5 for those thermocouples that pass through water or as 298 K (25 °C) for those thermocouples that pass through air. The heat-transfer coefficient is assumed to be 5 kW/m<sup>2</sup>·K for water and 0.1 kW/m<sup>2</sup>·K for air. Figure 8 specifies with an A or a W which thermocouples are adjusted for air and water, respectively.

Generally, the model and measurements match fairly well, usually within 10 K (5 pct error). The thermocouples

on the narrow faces nearest mold exit are overpredicted, but this is expected given that the CONID model was calibrated for the wide face. Some of the wide-face thermocouple measurements showed considerable asymmetry (30 K (30 °C) to 40 K (40 °C)) between the plates on the inner and outer radius, so deviations from the modeling predictions are expected at those locations. The outer radius wide-face measurements match much better with the model predictions than the inner radius, suggesting a difference between the inner radius and outer radius (the outer radius wide face generally had the higher temperatures). The larger mismatches occur in the funnel region near the meniscus, so the shell might be losing contact with the funnel more on one side than on the other.

## V. MOLD DISTORTION RESULTS

The primary focus of this study is the distortion behavior of the mold. In addition, the practical consequences are investigated regarding possible problems of tensile stress overloading of the bolts, bolt shearing at the mold-waterbox interface, narrow-face edge crushing, mold taper, and mold wear. In all results figures, increasingly positive values of displacement mean distortion further away from the molten steel, towards the mold cooling water, or further along the casting direction.

Figures 11 and 12 show the distorted shape of the narrow-face mold plates and waterbox. Expansion of the copper hot face is constrained by the cold face and waterbox, which causes the entire assembly to bow towards the molten steel into a roughly parabolic arc,

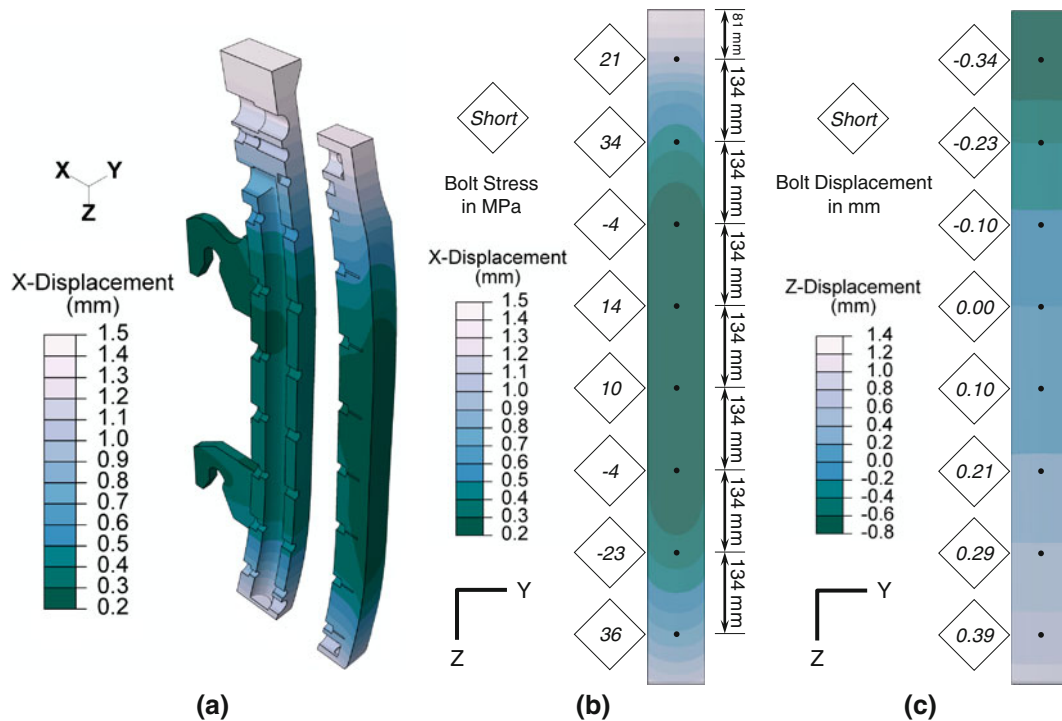


Fig. 12—(a) Narrow-face mold and waterbox distortion (50 times scaled distortion). (b) Narrow-face hot-face displacement away from SEN and bolt stresses. (c) Narrow-face hot-face and bolt displacement towards mold exit.

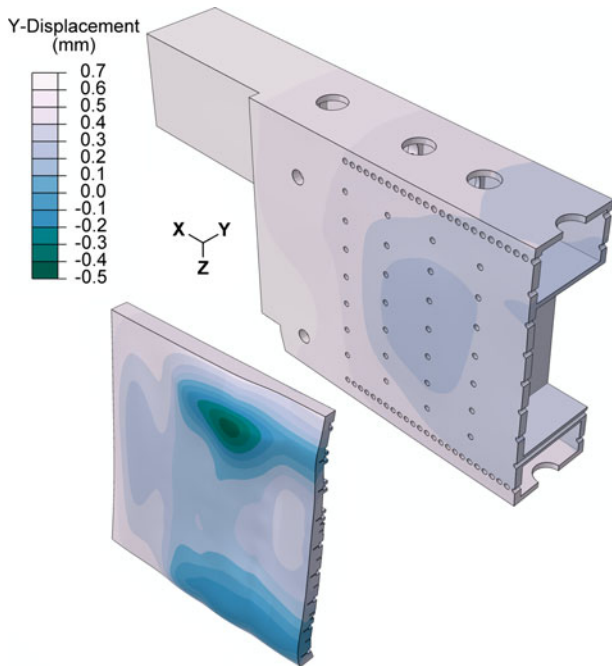


Fig. 13—Wide-face mold and waterbox distortion (50 times scaled distortion).

like a bimetallic strip. This classic behavior of the narrow face is expected and agrees with previous work.<sup>[7]</sup> About 0.9 mm difference is predicted between the maximum, found midway down the mold, and mold exit. The parabolic distortion has a slight wobble in the middle of the mold, caused by the extra rigidity of the waterbox hooks. Distortion across the thin perimeter direction is very small.

The distortion of the wide-face mold and waterbox is shown in Figures 13 through 19. In general, the thermal distortion causes the copper mold plates to bow towards the molten steel in the shape of a W, both vertically and horizontally. The mold also is pushed by the molten steel due to the ferrostatic pressure, but this effect is small. More importantly, the bolts through the waterbox constrain the thermal distortion of the mold plates, especially considering the shorter, stiffer bolts. The cold edges of the mold, *i.e.*, the top edge and the edge furthest from the centerline, provide constraint against some of the expansion that the hot-face experiences. The distortion is most pronounced just below the meniscus and towards mold exit, near where the surface temperatures are highest.

The central region of the wide-face mold, *i.e.*, the inner flat and inner curve regions, which in conventional slab molds experiences the most distortion,<sup>[7]</sup> has relatively little

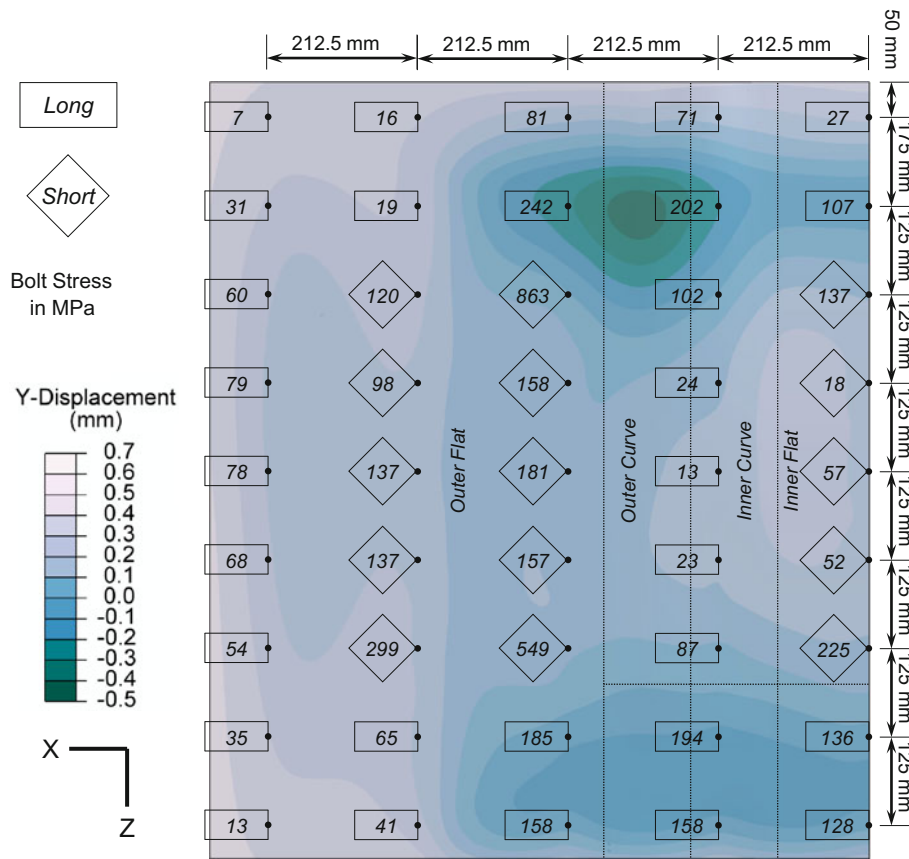


Fig. 14—Wide-face hot-face displacement away from steel and bolt stresses.

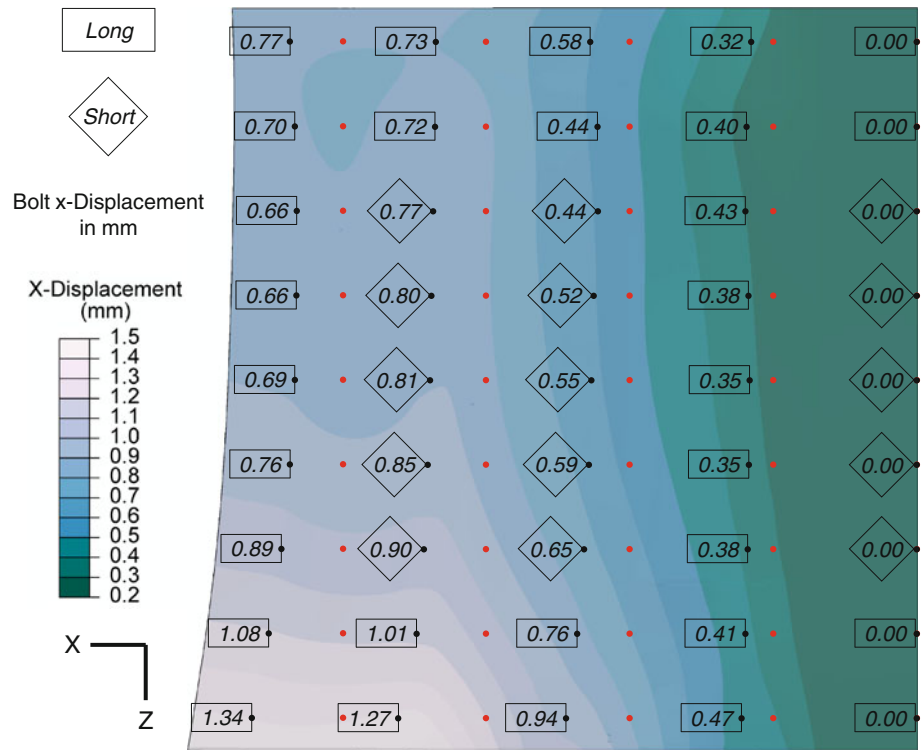


Fig. 15—Wide-face hot-face and bolt displacement towards narrow face (100 times scaled distortion in x-direction).

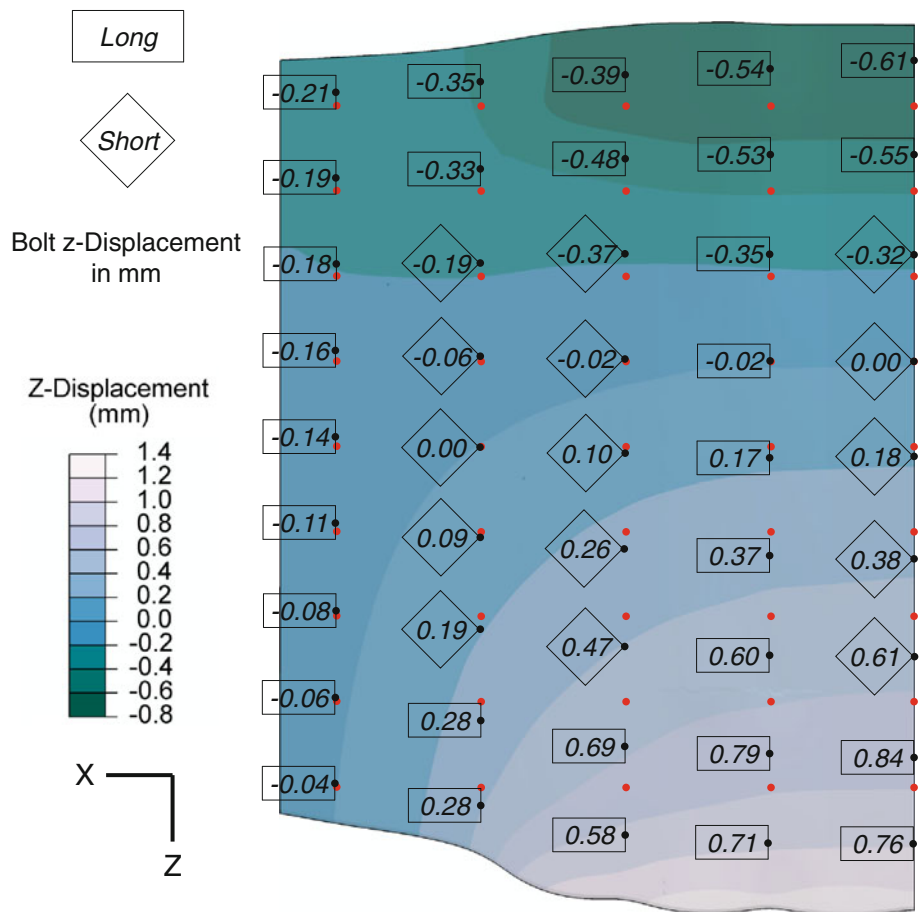


Fig. 16—Wide-face hot-face and bolt displacement towards mold exit (100 times scaled distortion in z-direction).

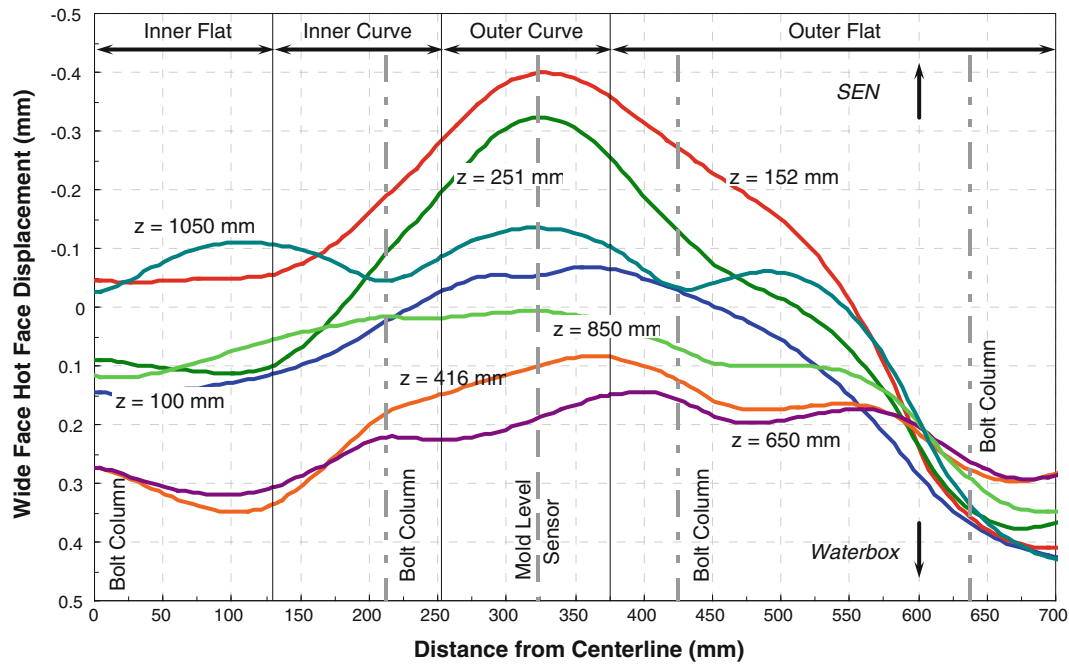


Fig. 17—Wide-face hot-face distortion profiles around the perimeter.

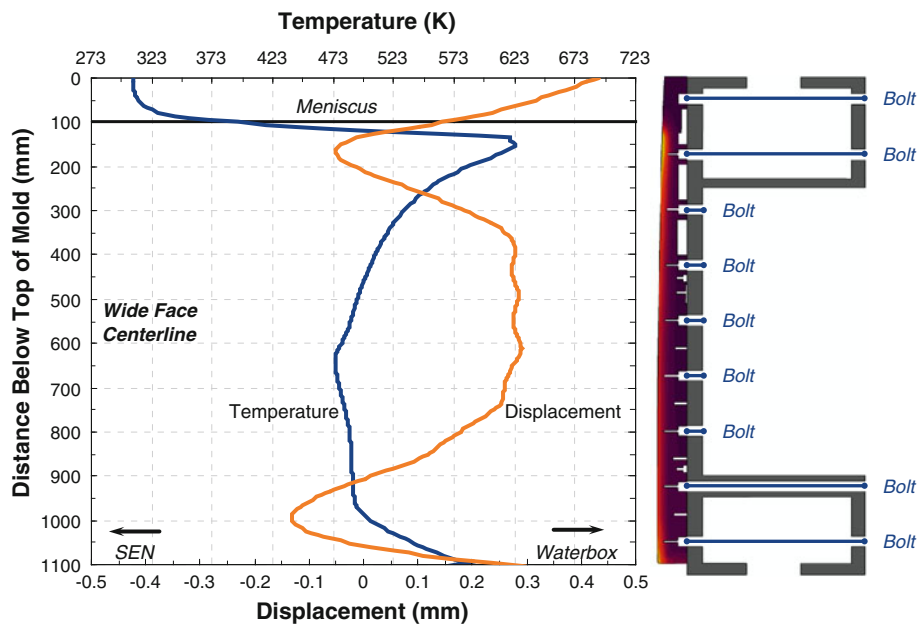


Fig. 18—Wide-face hot-face temperature and displacement at centerline.

distortion in this mold. This is due to the constraint provided by the short bolts, which connect the mold plates to the hollowed-out portion of this very rigid waterbox. The most severe distortion is found just below the meniscus in the middle of the outside curve region of the funnel at the same location as the mold-level sensor channel, but this is just a coincidence; the more relevant feature of this peak location is that it lies between two bolt columns, one of which consists only of long, compliant bolts. As shown in Table III, the longer bolts have only about 15 pct of the

stiffness of the shorter bolts. Except for the top two rows and bottom row of bolts, these longer bolts are attached to the mold through stiffener plates on the waterbox, which offset their lower stiffness. The peaks in mold distortion occur at 325 mm from the centerline at 200 and 1000 mm below mold top as shown in Figures 14, 17, and 19, in the vicinity of the long bolts without stiffener plates. The cavities for the electromagnetic flow control system thus have significant effect on the distorted shape of the mold.



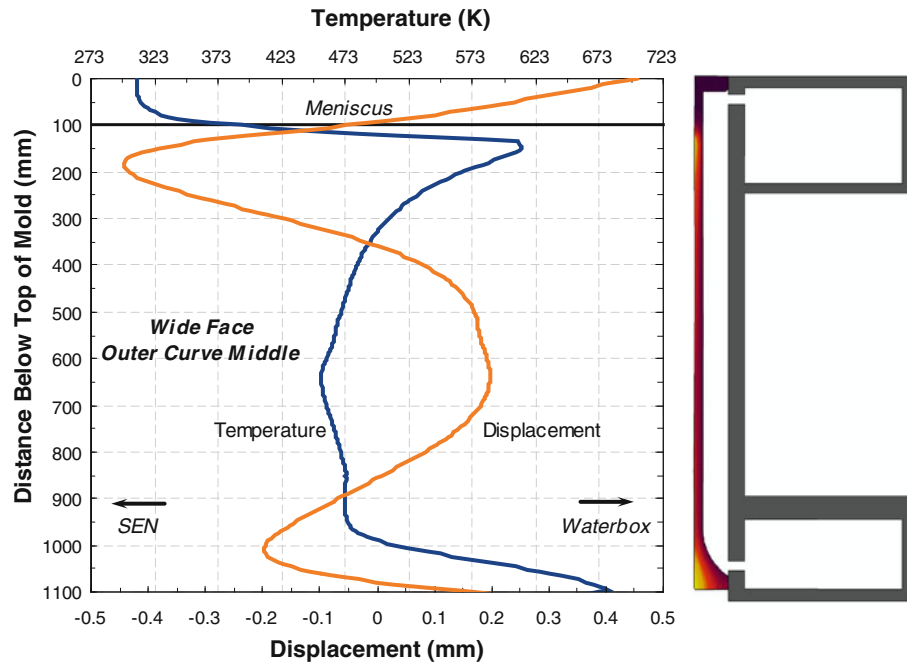


Fig. 19—Wide-face hot-face temperature and displacement at outer curve middle.

#### A. Bolt and Tie Rod Tensile Stresses

The boxes in Figures 12(b) and 14 present the operating tensile stresses of the mold bolts for the narrow and wide faces, respectively. For the narrow face, the highest bolt stresses are found near the top and bottom of the mold, where they partially restrain the most severe copper plate distortion, as shown in Figures 11 and 12. These stresses are not of practical consequence as they are well below the yield strength of the bolt material. The bolts aligned with the waterbox hooks are calculated to operate in compression because the additional stiffness provided by the hooks generates only a small operating load, which is not enough to overcome the prestress.

In the wide face, the bolts with the highest tensile stresses are the short bolts found 425 mm from the centerline at 300 and 800 mm below the top of the mold. The maximum tensile stresses are over 800 MPa and arise in the short bolts nearest to the locations of maximum distortion. Because the loading is strain controlled and not stress controlled, these stresses likely cause a small, permanent distortion of the steel bolts, which should not present any operational problems. Figures 18 and 19 show the temperature and distortion profiles down the wide-face hot face at the centerline, where the distortion is relatively small, and at the middle of the outer curve region, where the distortion is most severe. Near the top and bottom of the mold, where the thermal expansion is resisted by the compliant long bolts, the hot face distorts the most and the bolts develop moderate stresses. In the middle region of the mold, the expansion is resisted by the stiff short bolts, which develop high stresses, except for the column of long bolts 212.5 mm from the centerline. The variation

in bolt stiffness is largely responsible for the short bolts carrying most of the load and the local increase in hot-face distortion around the longer bolts.

The model predicts the tie rod operating tensile stresses to be 151 and 146 MPa for the upper and lower tie rods, which correspond to axial forces of 183 and 178 kN. This force exceeds what is applied in commercial practice but should not otherwise affect the reported model predictions.

#### B. Mold Lateral Distortion and Bolt Shearing

If lateral distortion of the copper plates relative to the waterboxes is excessive, then the resulting shear forces on the bolts may cause excessive mold constraint or even bolt failure. Figure 12(c) shows the in-plane distortion of the narrow-face hot face, which is mainly in the casting ( $z$ -) direction, as the copper plate elongates by about 2 mm. There is little risk of shearing the narrow-face bolts because the bolt holes are radially oversized by 3 mm (16 mm bolts in 22 mm holes) and the maximum in-plane displacements of the bolts at the mold–waterbox interface are less than 0.4 mm, as shown in the boxes in Figure 12(c).

Figures 15 and 16 show contours of the in-plane distortion of the wide-face mold, in the directions towards the narrow face ( $x$ -) and in the casting direction, respectively. The  $x$ -distortion is greatest at the bottom corner, while the  $z$ -distortion is greatest at the bottom center. This distorted shape is explained by the constraint against thermal distortion provided by the cold edges along the top and down the side of the mold. This has important implications for taper practice, as discussed later. The markers in Figures 15 and 16 indicate the initial and deformed position of the

bolt holes, and the boxes give the calculated bolt displacements at the mold–waterbox interface in the respective directions. The two bolts in the bottom row at 637.5 and 850 mm from the centerline have the highest total in-plane displacements  $u = \sqrt{u_x^2 + u_z^2}$  of 1.30 and 1.34 mm. As the bolt holes on the wide-face waterbox are radially oversized by 4 mm (16 mm bolts in 24 mm holes), there is again little risk of shearing failure of any bolts.

### C. Narrow-Face Edge Crushing and Fin Formation

Excessive clamping forces combined with mold distortion is known to cause crushing of the corner of the narrow face.<sup>[7]</sup> Figure 20 shows the model prediction of the normal displacement of the main line of contact between the narrow and wide faces, as well as two horizontal slices through the interface that show the distorted mold shape (no scaling of the distortion) with temperature contours. The meniscus experiences a small (0.2 mm) gap, which might entrap liquid mold flux that could solidify and cause scratching during width changes. The locations of the highest temperatures, just below the meniscus and near the mold exit, are in good contact because of the higher thermal expansion and the tie rod forces, while the regions in between experience a thin gap of 0.017 mm on average. The hash marks in the figure indicate the positions of the rows of bolts, which are not directly responsible for the gap profile.

Combined with excessive clamping forces, the corner of the narrow faces may be crushed at the two locations of high contact pressure. If the narrow-face copper corner heats excessively, softens, and permanently adopts to the crushed shape, then a large wedge-shaped residual gap can form at the location marked with the arrows in Figure 20 after the mold cools. During

subsequent startups, this gap may fill with slag or molten steel, causing “fin” problems, and it can lead to sticker breakouts in extreme cases.<sup>[7]</sup> These problems were not experienced in this plant, however. The model prediction of the corner heating and contact pressure is likely overpredicted because the contact between the mold pieces allows for some cooling of the narrow-face corners, which was ignored by the model treating the interface as perfectly thermally insulated.

### D. Implications for Mold Taper Design

Mold distortion need not be a problem, so long as it is understood and properly accounted for when constructing the mold and designing the taper practices. The variation down the mold of the mold hot-face shape affects the mold taper experienced by the solidifying and shrinking steel shell. The narrow face distorts about 1 mm, which is important relative to the typical taper of about 4 to 7 mm per narrow face. The wide face distorts about  $\pm 0.5$  mm, which is less consequential to wide-face taper because ferrostatic pressure can maintain contact of the large area of unsupported shell against the wide face.

A more important aspect of the wide-face distortion is the change in perimeter length caused by the distortion. This is quantified by subtracting the distorted perimeter length at the meniscus from the distorted perimeter length down the mold. The change in perimeter length of the wide-face mold has contributions from the changing funnel geometry, which decreases the perimeter, and the thermal distortion, which increases the perimeter. Because of this compensation provided by the thermal expansion at elevated temperatures, the total perimeter length change is smaller than what

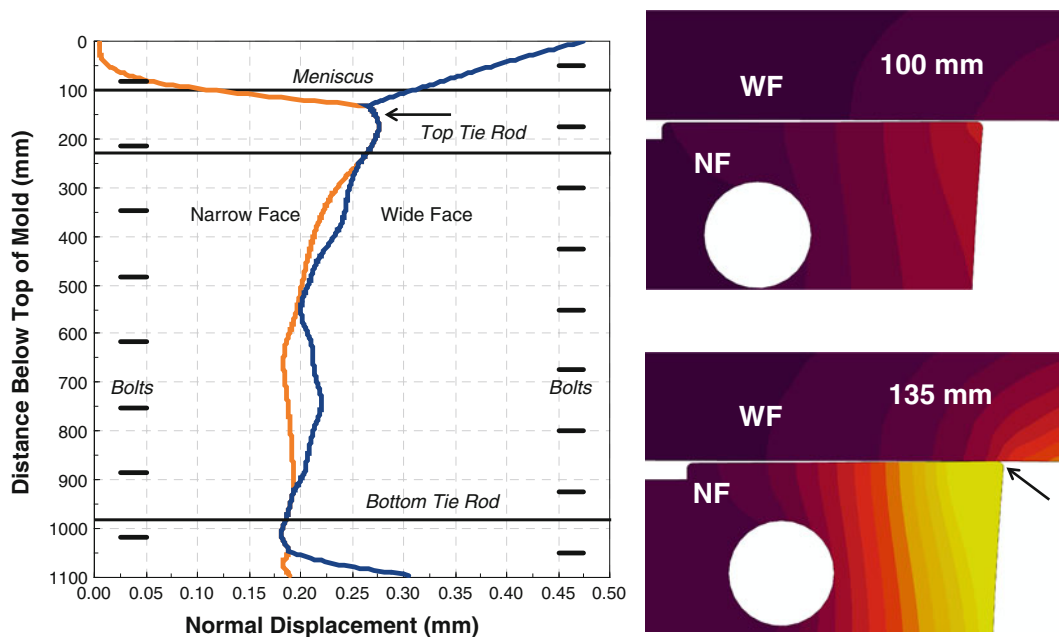


Fig. 20—Interfacial contact profile between mold faces.

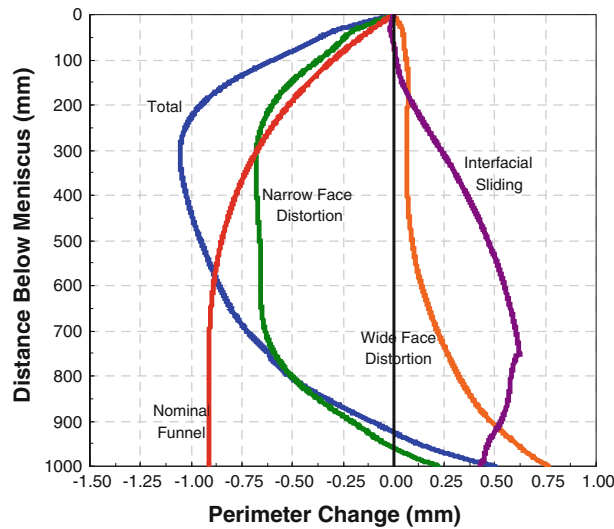


Fig. 21—Perimeter change due to distortion and funnel geometry.

calculations at ambient temperature would show. Figure 21 shows the effective shape of the mold experienced by the solidifying shell moving down the wide face (Total), as well as split into four components: the perimeter change of the wide face with the funnel geometry effect removed (Wide Face Distortion), the prevented sliding of the wide face relative to a rigid narrow face (Interfacial Sliding), the perimeter change due to the funnel geometry (Nominal Funnel), and the perimeter change due to the thermally changed narrow-face shape taken from Figure 11 (Narrow Face Distortion).

The total distortion from all four components should be considered when designing narrow-face taper of most clamped funnel-shaped molds, where narrow-face support is insufficient to prevent mechanical backlash and gaps from allowing the narrow face to move along with the wide-face expansion. In molds with rigidly positioned narrow faces, the edge of the narrow face that contacts the wide face may slide, so the “interfacial sliding” effect should not be considered. During operation of the mold with slab width changes during operation, the interfacial sliding effect is determined mainly during startup, due to the heat up from a cold mold to a hot mold. Online monitoring of the shape of the narrow-face mold by inclinometers is recommended to quantify these effects during casting operation and to ensure that optimal taper is maintained.

Under conditions of ideal taper, the tapered shape of the surface of the distorted narrow face should match the shrinkage of the solidifying steel down the wide face. Previous work<sup>[18,19]</sup> has investigated the shrinkage behavior of the solidifying shell in the funnel mold described in this work, using a two-dimensional elastic-viscoplastic thermal-stress model. Figure 22 shows the shell shrinkage down the narrow face predicted in this previous work both with and without friction (0.16 static friction coefficient between the shell and mold). These two shrinkage predictions are compared in Figure 22 with the perimeter changes of both the cold mold and the distorted mold calculated in this work. Both mold lines in Figure 22 include a 1 pct/m taper, which is 12 mm total for the 1200 mm strand width

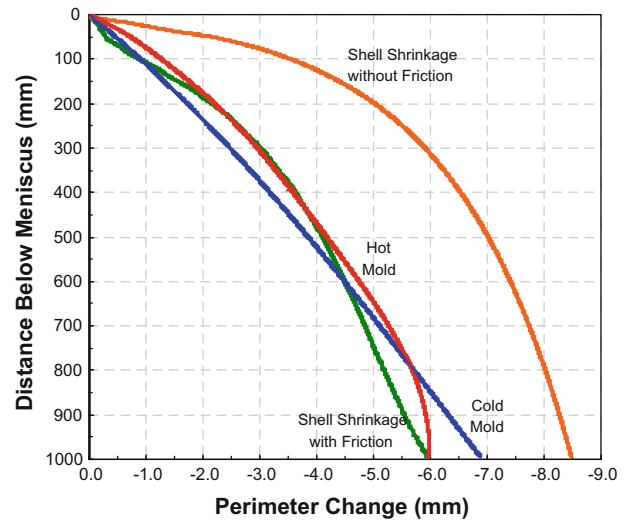


Fig. 22—Steel shell shrinkage with friction and mold distortion.

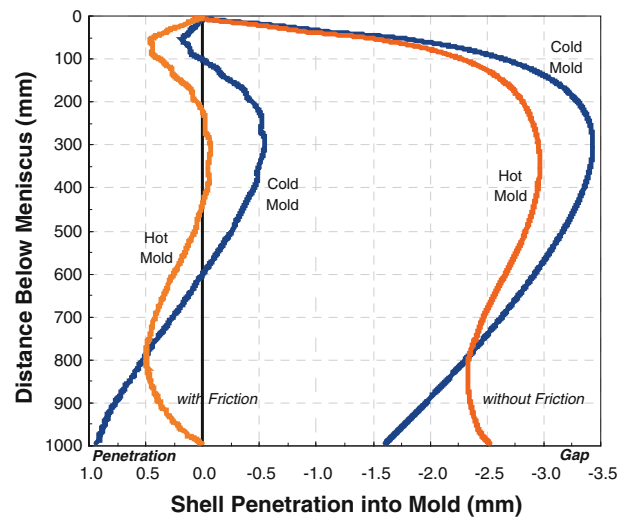


Fig. 23—Shell-mold gap with friction and mold distortion.

considered in this work. At room temperature, this is a straight line from the origin to 6 mm of shrinkage at 1000 mm below the meniscus in Figure 22. Ideally, this applied taper should make the mold shape match the shell shrinkage, and although not entirely ideal, this taper does a fairly good job when all effects are considered.

The deviation from ideal narrow-face taper is explored in Figure 23, which shows the difference between the mold lines and shell lines in Figure 22. In this figure, negative numbers mean that the shell is shrinking more than the applied narrow-face taper can accommodate, so a gap tends to form between the shell and the mold on the narrow face. Positive numbers mean that the shell is pushing against the narrow-face mold wall, which would cause excessive mold wear, and other problems, such as off-corner buckling of the shell and longitudinal cracks. This figure shows that mold

distortion and friction both greatly lessen the ideal narrow-face taper needed to match the shell shrinkage.

### E. Mold Wear

The narrow-face mold wear as a function of distance down the mold  $w(z)$  may be assumed to be composed of at least three phenomenological components: a constant term due to the “steady” wear of two bodies in sliding contact  $c_0$ , a linear term proportional to the ferrostatic pressure load  $c_1 p$ , and a third term due to the mismatch from ideal taper  $d(z)$ . These components are added together to give a crude estimate of the total narrow-face wear

$$w(z) = c_0 + c_1 \rho g z + d(z) \quad [15]$$

Measurements of narrow-face mold wear from the plant, shown in Figure 24, are consistent with taking the mismatch function  $d(z)$  as the “hot mold with friction” penetration profile presented in Figure 23. Good match with the measurements may be observed by taking  $c_0 = 0.97$  mm and  $c_1 = 5 \times 10^{-6}$  mm/Pa as fitting constants. Minimum wear is observed between 200 and 500 mm below the meniscus. The higher wear towards the top and bottom of the mold agrees with the modeling prediction of two regions of locally excessive taper and corresponding high narrow-face mold wear. The very high wear at mold exit is likely related to the combined effects of the infiltration of corrosive spray-cooling water, increased scraping by the strand at mold exit, and the softening caused by the locally high mold temperatures discussed in Section IV. This problem can be treated in many ways: changing the bolt pattern, changing bolt tightness or lubrication, stiffening the waterbox, or changing the narrow-face taper. Further modeling work is needed to optimize mold taper for the range of operating conditions in commercial practice.

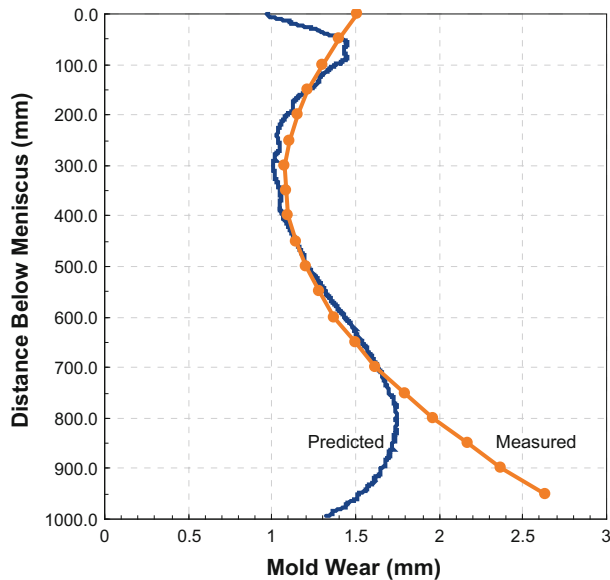


Fig. 24—Mold wear predictions and measurements.

## VI. CONCLUSIONS

This work provides insight into the thermal and mechanical behavior of a funnel-mold continuous caster during steady casting, based on a nonlinear 3-D finite-element elastic stress analysis. The model features realistic thermal boundary conditions based on plant measurements from a previous study, complete geometric details of the mold plates and waterboxes, tightened bolts and tie rods, and realistic contact with friction and ferrostatic pressure.

The behavior of the narrow face is typical, bowing into a parabolic arc. Owing to the changes in water cooling around the mold bolts and near mold exit on the wide face, combined with widely varying bolt stiffness, the wide face contorts into a W shape in both the perimeter and casting directions.

The results of the model were evaluated from an operational perspective, considering the potential for several different practical problems as follows:

1. The mold bolts have no risk of either tensile failure or shearing failure at the mold–waterbox interfaces, owing to the bolt holes being sufficiently oversized.
2. The mold pieces are in strong contact just below meniscus and just above mold exit, where the temperatures are highest. The meniscus region could experience scratching due to slag infiltration into a thin (0.2 mm) interfacial gap. The submeniscus region could experience the “crushing” phenomenon observed in previous work unless care is taken to avoid excessive clamping forces.
3. Mold distortion has a significant effect on mold taper. The thermal distortion of each of the mold pieces, the effect of the changing funnel geometry, and the interfacial sliding of the wide and narrow faces all contribute to the effective taper seen by the solidifying shell, each in a nonlinear fashion with distance down the mold. The thermal expansion of the wide face works against the applied taper and the effect of the funnel, so calculations based only on room-temperature dimensions are insufficient.
4. Mold wear was estimated by superimposing the total effect of the thermal distortion of the mold and a linear 1 pct/m taper on previous calculations of the shell behavior. Although this taper generally produces acceptable matching with the shell shrinkage, the shell is predicted to wear against the mold just below the meniscus and near mold exit. Plant measurements of mold wear are consistent with this prediction.
5. To avoid shell buckling and cracks, the thermal distortion of the mold should be considered when designing taper practice.

## VII. FUTURE WORK

To implement the results of this work into practice requires online monitoring of the shape of the narrow-face mold by inclinometers in order to quantify the mold distortion effects and actual taper experienced during casting operation. The computational models should be



fully coupled to include the effect of the mold distortion on the behavior of the solidifying steel shell and interfacial gap phenomena. Efforts to do this are currently underway, and a follow-up article is planned.

## ACKNOWLEDGMENTS

The authors gratefully acknowledge the financial support of the member companies of the Continuous Casting Consortium at the University of Illinois, as well as the computational resources provided by The National Center for Supercomputing Applications (NCSA) at the University of Illinois. The authors also thank personnel at the Tata Steel DSP for plant data and support.

## REFERENCES

1. I.V. Samarasekera and J.K. Brimacombe: *Iron & Steelmaker*, 1982, vol. 9, pp. 1–15.
2. I.V. Samarasekera, D.L. Anderson, and J.K. Brimacombe: *Metall. Trans. B*, 1982, vol. 13B, pp. 91–104.
3. I.V. Samarasekera and J.K. Brimacombe: *Metall. Trans. B*, 1982, vol. 13B, pp. 105–16.
4. J.-E. Lee, H.N. Han, K.H. Oh, and J.-K. Yoon: *ISIJ Int.*, 1999, vol. 39, pp. 435–44.
5. Y. Hebi, Y. Man, Z. Huiying, and F. Dacheng: *ISIJ Int.*, 2006, vol. 46, pp. 546–52.
6. Y.-M. Xie and S.-R. Yin: *J. Strain Anal. Eng. Design*, 2008, vol. 43, pp. 565–68.
7. B.G. Thomas, G. Li, A. Moitra, and D. Habing: *Iron & Steelmaker*, 1998, vol. 25, pp. 125–43.
8. X. Liu and M. Zhu: *ISIJ Int.*, 2006, vol. 46, pp. 1652–59.
9. J. Zhou, X. Peng, and Y. Qin: *Int. J. Adv. Manuf. Technol.*, 2009, vol. 42, pp. 421–28.
10. L.C. Hibbeler, K. Xu, B.G. Thomas, S. Koric, and C. Spangler: *Iron Steel Technol.*, 2009, vol. 6, pp. 60–73.
11. T.G. O'Connor and J.A. Dantzig: *Metall. Mater. Trans. B*, 1994, vol. 25B, pp. 443–57.
12. J.K. Park, I.V. Samarasekera, B.G. Thomas, and U.S. Yoon: *Metall. Mater. Trans. B*, 2002, vol. 33B, pp. 425–36.
13. J.K. Park, I.V. Samarasekera, B.G. Thomas, and U.S. Yoon: *Metall. Mater. Trans. B*, 2002, vol. 33B, pp. 437–49.
14. ABAQUS 6.9-1 User Manuals. 2009, ABAQUS Inc., Dassault Simulia, Inc., Providence, RI.
15. C.A. Sleicher and M.W. Rouse: *Int. J. Heat Mass Trans.*, 1975, vol. 18, pp. 677–83.
16. Y. Meng and B.G. Thomas: *Metall. Mater. Trans. B*, 2003, vol. 34B, pp. 685–705.
17. B. Santillana, L.C. Hibbeler, B.G. Thomas, A. Hamoen, A. Kamperman, and W. van der Knoop: *ISIJ Int.*, 2008, vol. 48, pp. 1380–88.
18. L.C. Hibbeler, B.G. Thomas, B. Santillana, A. Hamoen, and A. Kamperman: *Metall. Ital.*, 2009, vol. 6, pp. 1–10.
19. L.C. Hibbeler: Master's Thesis, University of Illinois, 2009.